

Journal of Biomedical Optics

BiomedicalOptics.SPIEDigitalLibrary.org

Noninvasively measuring oxygen saturation of human finger-joint vessels by multi-transducer functional photoacoustic tomography

Zijian Deng
Changhui Li

SPIE.

Zijian Deng, Changhui Li, "Noninvasively measuring oxygen saturation of human finger-joint vessels by multi-transducer functional photoacoustic tomography," *J. Biomed. Opt.* **21**(6), 061009 (2016), doi: 10.1117/1.JBO.21.6.061009.

Noninvasively measuring oxygen saturation of human finger-joint vessels by multi-transducer functional photoacoustic tomography

Zijian Deng and Changhui Li*

Peking University, Department of Biomedical Engineering, College of Engineering, No. 5 Yiheyuan Road, Haidian, Beijing 100871, China

Abstract. Imaging small blood vessels and measuring their functional information in finger joint are still challenges for clinical imaging modalities. In this study, we developed a multi-transducer functional photoacoustic tomography (PAT) system and successfully imaged human finger-joint vessels from ~ 1 mm to <0.2 mm in diameter. In addition, the oxygen saturation (SO_2) values of these vessels were also measured. Our results demonstrate that PAT can provide both anatomical and functional information of individual finger-joint vessels with different sizes, which might help the study of finger-joint diseases, such as rheumatoid arthritis. © 2016 Society of Photo-Optical Instrumentation Engineers (SPIE) [DOI: 10.1117/1.JBO.21.6.061009]

Keywords: photoacoustic tomography; human finger joints; oxygen saturation; medical imaging.

Paper 150707SSRR received Nov. 6, 2015; accepted for publication Apr. 19, 2016; published online May 12, 2016.

1 Introduction

Rheumatoid arthritis (RA) is a serious health threat, affecting 0.5% to 1% of the population in Northern Europe and North America.¹ The finger joint is a common location of this disease. RA is considered to be an angiogenesis-dependent disease,² and the neovascular network presents remarkable hypoxia in RA-affected joints.³ Thus, pharmacological inhibitors of angiogenesis may provide solutions to disease suppression.^{4,5} Therefore, the hyperplastic vessel and its hypoxia have the potential to be indicators for the diagnosis of RA. Although the finger joint has been studied by many clinical-imaging methods,⁶ such as x-ray radiography,⁷ x-ray computed tomography (CT),⁸ single photon emission CT (SPECT),⁹ ultrasonography,¹⁰ and magnetic resonance imaging (MRI),^{11,12} it is still a challenge to image small vessels in the joint. Photoacoustic tomography (PAT) is an emerging optical imaging modality that combines the optical absorption contrast with ultrasonic detection. PAT has proven superior in imaging blood vessels noninvasively, especially for high-resolution imaging of peripheral vessels.^{13–16} In addition, PAT can quantitatively measure the oxygen saturation (SO_2) at the single-vessel level.^{17,18} Several researchers have already used PAT to image finger joints. Wang et al.¹⁹ have reported two-dimensional photoacoustic images of the proximal interphalangeal (PIP) and distal interphalangeal (DIP) joints from a cadaver human finger. Sun et al.²⁰ have presented a three-dimensional (3-D) PAT technique that is able to image the DIP finger joints *in vivo* in a spherical scanning geometry. Ermilov et al.²¹ have demonstrated the feasibility of visualizing 3-D large finger blood vessels. van Es et al.²² have visualized the *in vivo* human-finger blood vessels across both interphalangeal joints.

In this study, we developed a PAT finger-joint imaging system. This system not only imaged different sizes of vessels in the finger joint but also measured their SO_2 values. Our work demonstrated that PAT could be a tool to measure the SO_2 in finger

joints, which might help the study of finger-joint diseases, such as rheumatoid arthritis.

2 Methods

2.1 Imaging System Setup

The finger-joint imaging system was shown in Fig. 1(a). This system employed an upside-down “bowl-like” acoustically penetrable optical reflector (APOR),²⁴ which allows the horizontally uniform ring-shaped light illumination. Ultrasound transducers were mounted on a ring-shaped rotational stage with a large central hole of 100 mm in diameter. During imaging, the forearm passed through the center hole, and the imaged index finger was firmly fixed downward by the finger holder. Transducers, the finger, and the APOR were all immersed in water. The illumination laser is a tunable Ti:sapphire laser system (LT-2211A, LOTIS TII, Minsk, Belarus), which generated laser pulses with ~ 12 -ns duration and 10-Hz repetition rate. Two wavelengths [as shown in Fig. 1(c)], 756 nm (a nonisobestic wavelength of hemoglobin) and 796 nm (an isobestic wavelength of hemoglobin), were used for functional imaging. The laser beam was delivered through the bottom of the water tank, which passed the conical lens to form a diverging ring-shaped light, then was reflected by APOR and irradiated on the finger-joint surface inwardly at a horizontal plane. The laser intensity at the surface of finger joint was <15 mJ/cm², which was below the American National Standards Institute limit.²⁵ During the imaging, both the finger and the APOR were maintained stable, while the photoacoustic (PA) signals were detected by two circularly scanned, cylindrically focused ultrasonic transducers. These two transducers have different central frequencies of 5 MHz (V307, Olympus NDT, Inc. Waltham, Massachusetts; element diameter: 25.4 mm, focal length: 54.2 mm, and numerical aperture: 0.228) and 10 MHz (V311, Olympus NDT, Inc., Waltham, Massachusetts; element diameter: 12.7 mm, focal

*Address all correspondence to: Changhui Li, E-mail: chli@pku.edu.cn

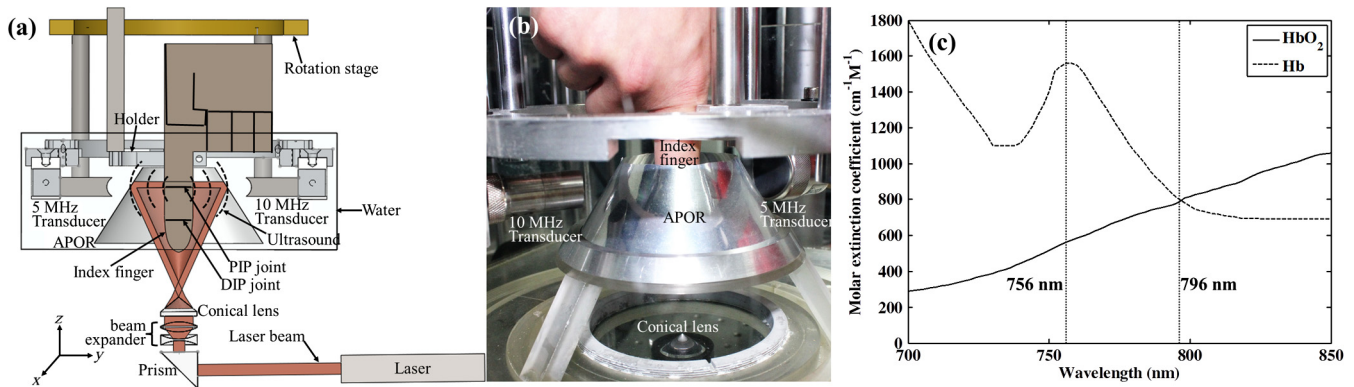


Fig. 1 (a) Experimental setup of the PAT system equipped with APOR. (b) A photograph of the experimental setup. (c) Molar extinction coefficient for hemoglobin in water.²³

length: 47.0 mm, and numerical aperture: 0.134), respectively. In order to acquire enough signal-to-noise ratio (SNR) and numerical aperture, we needed to choose the transducers with larger element sizes. The scanning speed is 3 min/round, and the scanning radius is about 50 mm. The signals were amplified 40 dB and recorded by a data-acquisition card (sampling rate: 100 MHz, CSE4327, DynamicSignals LLC, Lockport, Illinois). Both rotational stage and data acquisition were controlled by a LabVIEW program. After the PIP joint scanning, we raised the finger holder to adjust the DIP joint into the illuminated plane. PA images were reconstructed by the delay-and-sum algorithm.

2.2 Estimated Photoacoustic Tomography Spatial Resolution

Based on the parameters of these two transducers, the theoretical in-plane and z -axial resolutions of 5-MHz transducer were, respectively, calculated as 0.15 and 0.802 mm, and those theoretical resolutions of 10-MHz transducer were 0.075 and 0.683 mm, respectively. In the following, we performed two tests to estimate these two resolutions experimentally.

The thickness of the imaging slice was determined by the z -axial resolution, which was measured by detecting PA signals from a tiny copper particle (diameter of ~ 0.28 mm) along z -axis. In this experiment, the two transducers were fixed, and the copper particle moved along z -axis at a step size of

0.1 mm. Figure 2 presented the profile of peak-to-peak PA amplitudes from different z positions of the copper particle. After the Gaussian fitting, the full-width at half-maximum (FWHM) of the profile obtained by 5- and 10-MHz transducers was estimated to be 1.70 [Fig. 2(a)] and 1.04 mm [Fig. 2(b)], respectively.

To measure the horizontal in-plane resolution, we imaged three vertically mounted straight black hairs with a diameter of ~ 0.08 mm positioned at various distances from the center [Figs. 3(a) and 3(e)]. Due to the inwardly ring-shaped illumination, the PA signals of the central hair were much stronger than those of other hairs. Therefore, we added 0.05% intralipid as scattering media into coupling water for generating a more homogeneous photons distribution. Some distortion occurred around the hair positioned in the center. Actually, it was very difficult to perfectly align ring-shaped light coaxially to a rotational stage with an outer diameter of 183.88 mm. In addition, the coaxial alignment between central hair and ring-shaped light was easier than that between central hair and rotational stage. Therefore, the central hair was about 2 mm away from the rotational center. The blurring caused by the large element size distorted the image of the out-of-center hair.

The FWHMs of imaging results by 5- and 10-MHz transducers were shown in Figs. 3(b)–3(d) and 3(f)–3(h), respectively. The radial resolutions were kept relatively constant at difference positions, while the lateral resolutions slightly decreased with the increasing distance, which is consistent with Ref. 26.

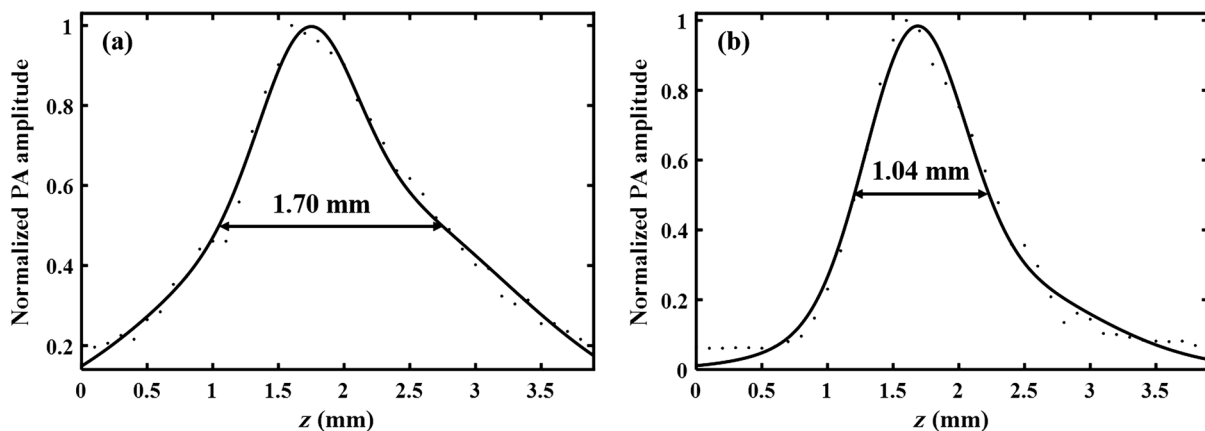


Fig. 2 Normalized PA amplitude values from a copper particle versus z position by cylindrically focused ultrasonic transducers with (a) 5-MHz and (b) 10-MHz central frequency.

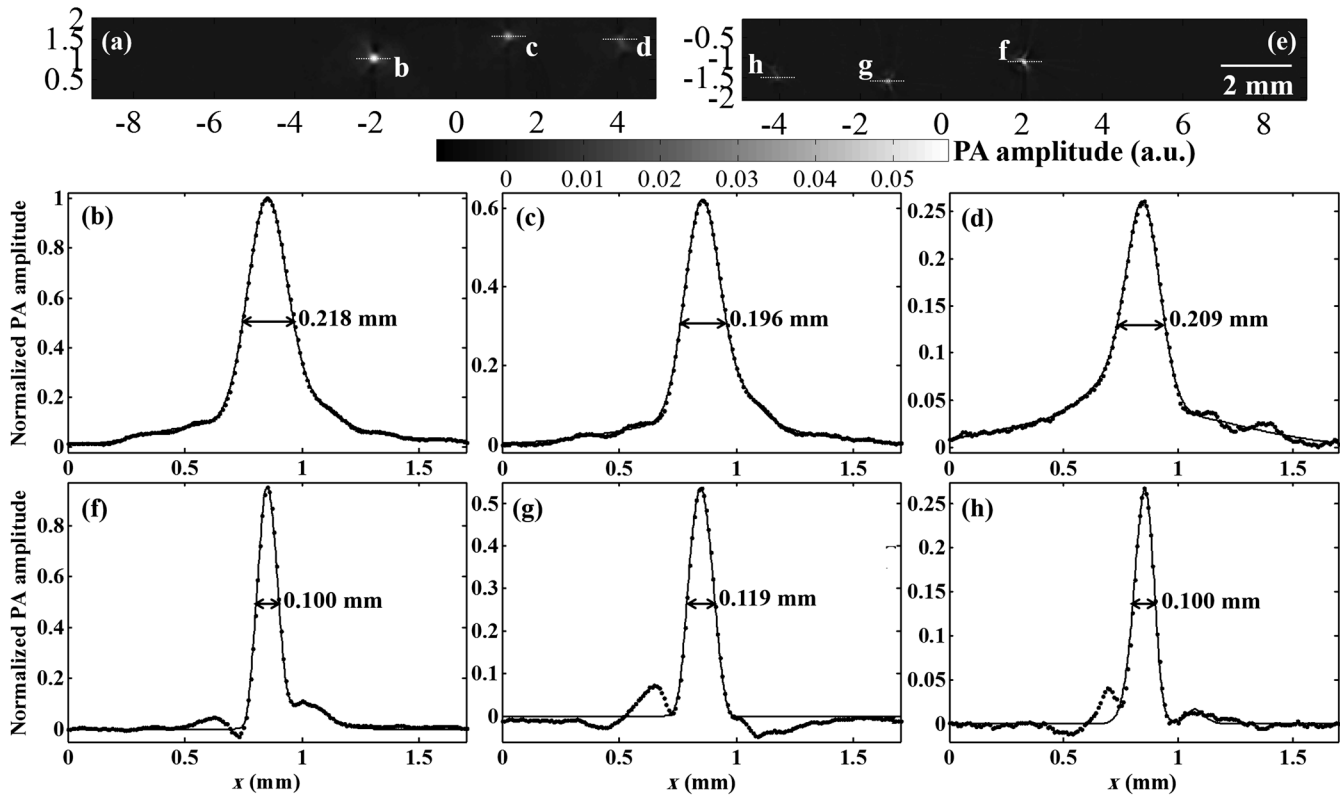


Fig. 3 Cross-sectional images of three black hairs with a diameter of ~ 0.08 mm positioned at various distances from the center, and their profiles along white dotted lines by cylindrically focused ultrasonic transducers with (a)–(d) 5-MHz and (e)–(h) 10-MHz central frequency.

However, since the radius of the finger was much less than the scanning radius, the lateral resolution was still comparable to the radial resolution, which would not cause serious deformation in the reconstructed vessels.

3 Imaging Results

In general, the optical attenuation in tissue is spectrally dependent. In this study, we used a two-layer model²⁷ to analyze the variation of local fluence, as described as follows:

$$F(\lambda) = F_0 \exp[-z_e \mu_{\text{eff}}^e(\lambda) - z_d \mu_{\text{eff}}^d(\lambda)], \quad (1)$$

where F_0 is the optical fluence on skin; z_e and z_d are the thicknesses of the epidermis and dermis above the vessels to be imaged, respectively; μ_{eff}^e and μ_{eff}^d are the effective optical attenuation coefficients in the epidermis and dermis, respectively. According to parameters in Ref. 27, the effective optical attenuation coefficients were calculated to be $\mu_{\text{eff}}^{e, 756 \text{ nm}} = 27.41 \text{ cm}^{-1}$, $\mu_{\text{eff}}^{e, 796 \text{ nm}} = 24.20 \text{ cm}^{-1}$, $\mu_{\text{eff}}^{d, 756 \text{ nm}} = 1.562 \text{ cm}^{-1}$, and $\mu_{\text{eff}}^{d, 796 \text{ nm}} = 1.432 \text{ cm}^{-1}$. The thicknesses of skin were set to be $z_e = 0.2$ mm and $z_d = 1.5$ mm, and then we can calculate the fluence ratio $F(756 \text{ nm})/F(796 \text{ nm}) = 0.9195$. This result was used for compensating the fluence variance in calculating SO_2 from PAT results of two wavelengths.¹⁷

This study was approved by the Institutional Review Board of Peking University, and all subjects provided written informed consent. The cross sections of the PIP and DIP joints of the right-hand index fingers of a 26-year-old healthy male volunteer were imaged by PAT (as shown in Fig. 4). By using transducer with 5-MHz center frequency, the blood vessels, even those about 0.5 mm in diameter, could show high contrast in PAT

images [Figs. 4(a#), and 4(d#)]. In the SO_2 measurement, we first manually coregistered regions of candidates from two images at 756 and 796 nm, which were “look-alike” vessels according to the relative contrast to nearby region and the “close-to-circular” shape. Then, we calculated the SO_2 of these candidates. Previous knowledge shows that the SO_2 of arteries and veins are around 0.98 and 0.75, respectively. Based on this knowledge, we set a window 0.65 to 1.05 to filter out those regions with abnormal SO_2 values.

We finally mapped the SO_2 on the PA image of 756 nm [as seen in Figs. 4(c) and 4(f)]. In this way, the types of joint vessels can be visually distinguished from their SO_2 values.

The 10-MHz transducer in PAT system was employed to image the smaller vessels in finger joints. Figures 4(g) and 4(j) presented the zoom-in results by 10-MHz transducer with the same positions shown in red dashed boxes of Figs. 4(a) and 4(d), respectively. Small vessels < 0.2 mm in diameter could be visualized in Figs. 4(g#) and 4(j#). We then calculated the SO_2 of the smaller joint vessels and similarly mapped the SO_2 on images of 756 nm [Figs. 4(i) and 4(l)]. Combining the results using two transducers [Figs. 4(i) and 4(l)], we could obtain the SO_2 maps of joint vessels with diameters from ~ 1 mm to < 0.2 mm.

In this PAT system, the transducers mounted on the system were relatively large (25.4 and 12.7 mm diameters of 5- and 10-MHz transducers, respectively), which might induce some smearing artifacts after reconstruction. However, the smearing artifact is generally caused by limited view. With the scanning radius of ~ 50 mm, the acquisition area of the transducer covered most of the entire finger (whose diameter was ~ 20 mm). Therefore, less-smearing artifacts existed within

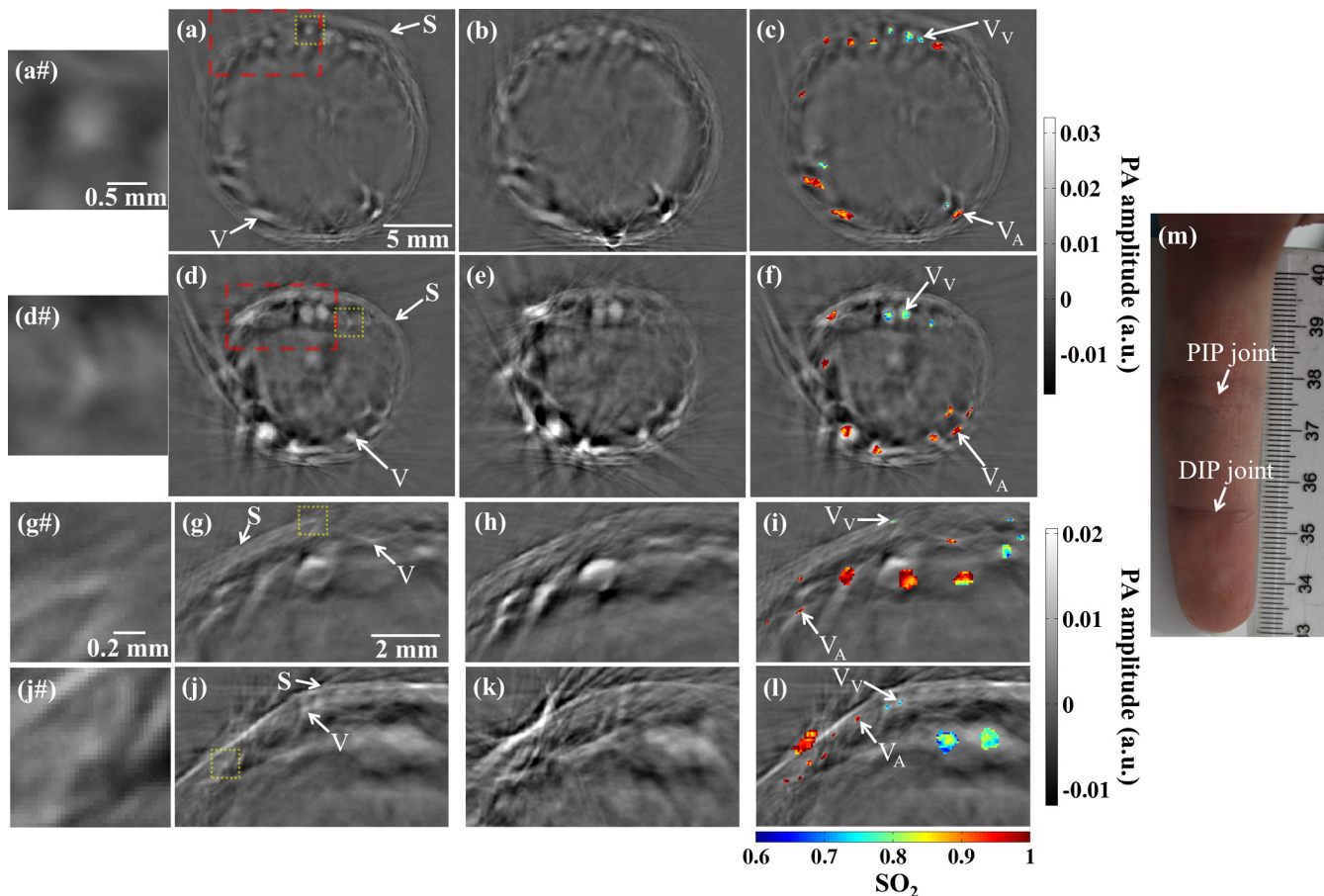


Fig. 4 Cross-sectional PAT imaging of right-hand index finger joints of a healthy male volunteer. Results of 5-MHz transducer: (a) PIP joint at 756 nm; (b) PIP joint at 796 nm; (c) SO_2 map of PIP joint overlaid on (a); (d) DIP joint at 756 nm; (e) DIP joint at 796 nm; (f) SO_2 map of DIP joint overlaid on (d); (a#) (d#) zoom-in images from yellow dotted box in (a) and (d), respectively, showing small vessels <0.5 mm in diameter. Results of 10-MHz transducer in the same position of corresponding joints shown in red dashed boxes at (a) and (d), respectively: (g) PIP joint at 756 nm; (h) PIP joint at 796 nm; (i) SO_2 map of PIP joint obtained by 5-MHz (bigger) and 10-MHz (smaller) transducers [overlaid on (g)]; (j) DIP joint at 756 nm; (k) DIP joint at 796 nm; (l) SO_2 map of DIP joint obtained by 5-MHz (bigger) and 10-MHz (smaller) transducers [overlaid on (j)]; (g#) (j#) zoom-in images from yellow dotted box in (g) and (j), respectively, showing small vessels <0.2 mm in diameter. (m) A photograph of the index finger. V, vessel; S, skin; VA, artery; and VV, vein.

the reconstructed finger regime, while it could be obvious if part of the finger was outside the acquisition region [as seen in the left side of Fig. 4(d)]. To reduce the influence of this artifact on the SO_2 calculation, we did not choose those vessel candidates close to the strong artifacts.

The acoustic reflections from the bone would affect the obtained images. However, the general convex surface of the bone would disperse the waves to a wider angle, which significantly decreased the energy of these reflected waves reaching the transducer. In addition, reflected ultrasound wave traveled more time to the transducer, which would affect the image reconstruction for deeper regions. In this study, we focused on the study of peripheral vessels. Therefore, the reflections would not play an important role in this study.

4 Summary and Discussions

The SO_2 of individual vessels from ~ 1 mm to <0.2 mm in diameter in human finger joints can be acquired via a PAT system equipped with 5- and 10-MHz transducers. According to the SO_2 values, the types of these vessels could be distinguished.

Our results suggested that the functional PAT could be used as a tool to study SO_2 of individual vessels in finger-joint RA patients.

However, the imaging speed of this system is relatively slow (3 min/round). Therefore, even aided with the affiliated finger holder, it is almost inevitable to have unintended movement during imaging. This movement would cause image blurring, or even mismatching between two images of different wavelengths or transducers. It is desired to employ more transducers or ultrasonic arrays, as in Ref. 28, to reduce the single-slice imaging time from minutes to seconds. In addition, since PAT can provide both anatomical and functional information of vasculature, integrating PAT with other imaging methods, such as CT and MRI, would become a powerful clinical imaging tool for patients with joint diseases.

Acknowledgments

This work was supported by the Doctoral Fund of the Ministry of Education of China (No. 20130001110035), the National Key Instrumentation Development Project (Nos. 2011YQ030114

and 2013YQ030651), and the National Science Foundation of China (No. 30831160516).

References

1. Y. Alamanos and A. A. Drosos, "Epidemiology of adult rheumatoid arthritis," *Autoimmune Rev.* **4**(3), 130–136 (2005).
2. R. A. Fava et al., "vascular-permeability factor endothelial growth-factor (VPF/VEGF)—accumulation and expression in human synovial-fluids and rheumatoid synovial tissue," *J. Exp. Med.* **180**(1), 341–346 (1994).
3. P. C. Taylor and B. Sivakumar, "Hypoxia and angiogenesis in rheumatoid arthritis," *Curr. Opin. Rheumatol.* **17**(3), 293–298 (2005).
4. P. R. Colvillanash and D. L. Scott, "Angiogenesis and rheumatoid-arthritis—pathogenic and therapeutic implications," *Ann. Rheum. Dis.* **51**(7), 919–925 (1992).
5. D. A. Walsh, "Angiogenesis and arthritis," *Rheumatology* **38**(2), 103–112 (1999).
6. M. Ostergaard, B. Ejbjerg, and M. Szkudlarek, "Imaging in early rheumatoid arthritis: roles of magnetic resonance imaging, ultrasonography, conventional radiography and computed tomography," *Best Pract. Res. Clin. Rheumatol.* **19**(1), 91–116 (2005).
7. M. Rahmani et al., "Detection of bone erosion in early rheumatoid arthritis: ultrasonography and conventional radiography versus non-contrast magnetic resonance imaging," *Clin. Rheumatol.* **29**(8), 883–891 (2010).
8. G. Peluso et al., "Detection of bone erosions in early rheumatoid arthritis: 3D ultrasonography versus computed tomography," *Clin. Rheumatol.* **34**(7), 1181–1186 (2015).
9. B. Ostendorf et al., "Early detection of bony alterations in rheumatoid and erosive arthritis of finger joints with high-resolution single photon emission computed tomography, and differentiation between them," *Skeletal Radiol.* **39**(1), 55–61 (2010).
10. F. Salaffi et al., "Inter-observer agreement of standard joint counts in early rheumatoid arthritis: a comparison with grey scale ultrasonography preliminary study," *Rheumatology* **47**(1), 54–58 (2008).
11. B. J. Ejbjerg et al., "Optimised, low cost, low field dedicated extremity MRI is highly specific and sensitive for synovitis and bone erosions in rheumatoid arthritis wrist and finger joints: comparison with conventional high field MRI and radiography," *Ann. Rheum. Dis.* **64**(9), 1280–1287 (2005).
12. A. Savnik et al., "MRI of the wrist and finger joints in inflammatory joint diseases at 1-year interval: MRI features to predict bone erosions," *Eur. Radiol.* **12**(5), 1203–1210 (2002).
13. X. D. Wang et al., "Noninvasive laser-induced photoacoustic tomography for structural and functional in vivo imaging of the brain," *Nat. Biotechnol.* **21**(7), 803–806 (2003).
14. G. Ku et al., "Multiple-bandwidth photoacoustic tomography," *Phys. Med. Biol.* **49**(7), 1329–1338 (2004).
15. P. Beard, "Biomedical photoacoustic imaging," *Interface Focus* **1**(4), 602–631 (2011).
16. L. H. V. Wang and S. Hu, "Photoacoustic tomography: in vivo imaging from organelles to organs," *Science* **335**(6075), 1458–1462 (2012).
17. H. F. Zhang et al., "Imaging of hemoglobin oxygen saturation variations in single vessels in vivo using photoacoustic microscopy," *Appl. Phys. Lett.* **90**(5), 053901 (2007).
18. J. Laufer et al., "In vitro measurements of absolute blood oxygen saturation using pulsed near-infrared photoacoustic spectroscopy: accuracy and resolution," *Phys. Med. Biol.* **50**(18), 4409–4428 (2005).
19. X. D. Wang, D. L. Chamberland, and D. A. Jamadar, "Noninvasive photoacoustic tomography of human peripheral joints toward diagnosis of inflammatory arthritis," *Opt. Lett.* **32**(20), 3002–3004 (2007).
20. Y. Sun, E. Sobel, and H. Jiang, "Quantitative three-dimensional photoacoustic tomography of the finger joints: an in vivo study," *J. Biomed. Opt.* **14**(6), 064002 (2009).
21. S. Ermilov et al., "Optoacoustic angiography of peripheral vasculature," *Proc. SPIE* **8223**, 82230D (2012).
22. P. van Es et al., "Initial results of finger imaging using photoacoustic computed tomography," *J. Biomed. Opt.* **19**(6), 060501 (2014).
23. S. Prahl, "Optical absorption of hemoglobin," <http://omlc.org/spectral/hemoglobin/>
24. Z. J. Deng et al., "Acoustically penetrable optical reflector for photoacoustic tomography," *J. Biomed. Opt.* **18**(7), 070503 (2013).
25. A. N. S. Institute, "American national standard for safe use of lasers," in *Z136.1-2000* A. N. S. Institute, ANSI Standard, New York (2000).
26. M. Xu and L. V. Wang, "Analytic explanation of spatial resolution related to bandwidth and detector aperture size in thermoacoustic or photoacoustic reconstruction," *Phys. Rev. E* **67**(5), 056605 (2003).
27. K. Maslov, H. F. Zhang, and L. V. Wang, "Effects of wavelength-dependent fluence attenuation on the noninvasive photoacoustic imaging of hemoglobin oxygen saturation in subcutaneous vasculature in vivo," *Inverse Prob.* **23**(6), S113–S122 (2007).
28. J. Gamelin et al., "A real-time photoacoustic tomography system for small animals," *Opt. Express* **17**(13), 10489–10498 (2009).

Zijian Deng is a PhD candidate in the Department of Biomedical Engineering, College of Engineering, Peking University. His research focuses on developing photoacoustic tomography techniques and its biomedical applications.

Changhui Li is an assistant professor in the Department of Biomedical Engineering at Peking University. He obtained his PhD at Texas A&M University in 2006, and then he continued his postdoctoral research in the Department of Biomedical Engineering at Washington University in St. Louis, Missouri. His research focuses on imaging methods in biomedicine, including photoacoustic tomography (PAT), fluorescence imaging, and molecular imaging.